Damage initiation and propagation assessed from stress-induced microseismic events during a mine-by test in the Opalinus Clay

Yves Le Gonidec, J. Sarout, Jérôme Wassermann, Christophe Nussbaum

Damage initiation and propagation assessed from stress-induced microseismic events during a mine-by test in the Opalinus Clay

Y. Le Gonidec,[1] J. Sarout,[2] J. Wassermann[3] and C. Nussbaum[4]

[1] *Géosciences Rennes, Université de Rennes* 1, *UMR* 6118 *CNRS, F*-35000 *Rennes, France.* E-mail: *Yves.LeGonidec@univ-rennes1.fr*
[2] *CSIRO, Earth Science and Resource Engineering, Perth, Australia*
[3] *Géosciences et Environnement Cergy, University of Cergy-Pontoise, France*
[4] *Swisstopo, Federal Office of Topography, CH*-3084 *Wabern, Switzerland*

SUMMARY
We report in this paper an original analysis of microseismic events (MSEs) induced by an excavation operation in the clay environment of the Mont Terri underground rock laboratory. In order to identify the MSEs with confidence, we develop a restrictive but efficient multistep method for filtering the recorded events. We deduce the spatial distribution and processes associated with the excavation-induced damage from the spatial location and focal mechanisms of the MSEs. We observe an asymmetric geometry of the excavation damaged zone around the excavated gallery, without notable microseismic activity in the sandy facies sidewall, in contrast with the shaly facies sidewall where a first burst of events is recorded, followed by two smaller bursts: one locates ahead of the excavation front and is associated with a dominant double-couple component, suggesting bedding plane reworking, that is, shear fracture mode, and the MSEs of the other cluster inside the shaly sidewall of the gallery, with a dominant compensated linear vector dipole component, suggesting extensive cracking. We identify and discuss four major factors that seem to control the MSEs source mechanisms: lithology, geometry of the geological features, gallery orientation and direction of the main compressive stress.

Key words: Geomechanics; Microstructures; Defects; Wave propagation; Acoustic properties.

1 INTRODUCTION

Damage in solids has major implications in many research fields. In Earth sciences, damage embraces several length scales, from dislocations in crystals, to microcracks/cracks, fractures/macrofractures and faults in geological structures (Weiss 2003). Multiscale damage processes that lead to the degradation of physical properties in rock mass structures (e.g. Lemaître 1990) is problematic in geomechanics, and can have far-reaching consequences for underground activities. Indeed, damage occurs in the rock mass surrounding an excavation, that is, notable perturbations of physical, mechanical and hydraulic properties are induced by the tunneling technique (blasting, header rod, etc.), local modifications of the stress field and, sometimes in the case of sedimentary rocks, desaturation phenomena (Tsang *et al.* 2012). The vicinity of the excavation where such damage takes place is the so-called excavation damaged zone (EDZ, e.g. Martino & Chandler 2004).

The knowledge of the EDZ in terms of initiation, extension and evolution in both space and time is of primary importance to ensure safety in underground galleries. In mining applications for instance, engineers limit the EDZ impact on the stability of the mine pillars by excavating in specific directions with respect to the rock mass structures, such as joints and bedding planes (Brady & Brown 1993). In the context of nuclear waste disposals into geological repositories, the EDZ constitutes a potential pathway for radionuclides to escape through the geological barriers towards ground water reservoirs for instance. Thus, monitoring the EDZ is required to ensure the feasibility of such repositories. Long-term stability and confining properties of host formations have been recently studied through mine-by tests performed in various underground research laboratories (URL). The extent of the EDZ can be assessed through the estimation of its transport properties (Martino & Chandler 2004): hydraulic and pneumatic methods, including hydraulic conductivity measurements in boreholes, are used to delineate the EDZ (Jakubick & Franz 1993; Souley *et al.* 2001; Bossart *et al.* 2002; Wassermann *et al.* 2011), or can be completed by core drilling analysis (e.g. Bossart *et al.* 2002) and visual inspection of the tunnel walls (Martin 1997; Cabrera *et al.* 1999; Nussbaum *et al.* 2011). Such methods, which are efficient to better understand the EDZ transport properties (Bossart *et al.* 2002; Bastiaens *et al.* 2007), remain localized and invasive. Complementary methods are thus required to ensure long-term monitoring of the EDZ.

Features characterizing the EDZ, such as spalling, notching, onion-like fracturing and pillar collapse in its dramatic form (Szwedzicki 2003), are related to local cohesion losses of the rock mass surrounding the excavation (Martin 1997) that can potentially radiate elastic energy. This sudden release of energy induces acoustic emissions (AEs) or, at larger scales, microseismic events (MSEs). Providing a non-destructive method for monitoring the physical properties and damage mechanisms inside the rock mass is therefore critical. Monitoring and analysis of microseismicity is largely used to predict rock-bursts or mining-induced catastrophes associated with stress redistribution and rock mass readjustments (Spottiswoode 1988; Young *et al.* 1992; Poplawski 1997; McGarr & Simpson 1997; Senfaute *et al.* 1997; Lynch & Mendecki 2001). Note that seismic velocity measurements, commonly used to determine the physical properties of a rock mass, can also be used to assess the stress redistribution (e.g. Maxwell & Young 1996; Sato *et al.* 2000), but require the use of active sources. Microseismic activity and source localization constitute passive means for quantifying damage (Scholz 1968) and estimating its spatial and temporal distribution at a metric scale, using acoustic sensor arrays (Falls & Young 1998; Cai *et al.* 2001). Finally, damage mechanisms can be assessed from controlled experiments (Feignier & Young 1992), which is not straightforward *in situ* due to the limited coverage of the damaged rock mass by acoustic sensors – but is ideal for small scale laboratory experiments where sensors can be placed all around the rock sample.

In the case of damage in brittle rocks (crystalline rocks), AE/MSE activity is often strong and makes the method very efficient to assess stress-induced damage mechanisms. Many studies have been reported in the literature, mainly based on AE laboratory experiments (Scholz 1968; Lockner *et al.* 1991; Lei *et al.* 1992; Chow *et al.* 1995; Rao & Kusunose 1995; Lei *et al.* 2000; Zang *et al.* 2000; Schubnel *et al.* 2003). For *in situ* experiments, mine-by tests have been performed in the Lac du Bonnet granite (URL located in Canada) where a strong correlation between MSE activity, stress concentration and strain localization has been observed (Baker & Young 1997; Cai *et al.* 2001; Young & Collins 2001; Martino & Chandler 2004). In contrast, very few microseismic studies, especially involving analysis of source mechanisms, have been published for shales or clay-rich rocks, whether at the laboratory (Sarout *et al.* 2010; Amann *et al.* 2012) or at the field scale (Forney 1999; Le Gonidec *et al.* 2012). The lack of data is related to the difficulty in recording MSEs: i) the microseismic response to stress perturbations, related to the fracture toughness parameter and to the brittle-to-ductile transition threshold, is inherently weaker for clay-rich rocks than for crystalline rocks, and ii) the strong intrinsic anisotropy of clay-rich rocks, associated to their bedding structure is believed to strongly attenuate seismic waves, mainly perpendicularly to the bedding planes (David *et al.* 2007). Therefore, less and weaker MSEs are expected in a shaly as opposed to crystalline rock for a given stress perturbation. If MSEs do exist in shales, they would be more difficult to detect and record with a reasonable signal-to-noise (S/N) ratio. Despite the data scarcity, shale formations are considered as relevant candidates for underground radioactive waste storage due to their extremely low permeability and to their sealing and self-healing capacity (Bastiaens *et al.* 2007; Blümling *et al.* 2007; Zhang & Rothfuchs 2008; Zhang 2011). In this context, various aspects of the Opalinus and Callovo-Oxfordian Clay formations sampled by the Mont Terri (Switzerland) and Bure (France) URLs, respectively, are being extensively investigated.

Recent microseismic studies aim at overcoming the obvious scarcity of information in this field and assessing the feasibility of

the method for remote and long-term monitoring purposes. Hence, we report here an original field investigation involving active (seismic survey) and passive (microseismicity) acoustic monitoring of the argillaceous formation of Mont Terri's URL during and following the excavation of an underground gallery. Details of the organization and first outcomes of the whole research program have been reported in earlier publications (Nicollin *et al.* 2010; Le Gonidec *et al.* 2012; Maineult *et al.* 2013). In the present article, we focus on the careful post-processing of the catalogue of MSEs recorded during the experiment, leading to a reliable spatio-temporal location and a first assessment of the associated damage mechanisms. Section 2 recalls the geological context and the principles of the acoustic experiments. In Section 3, the raw data set of events is reported along with the criteria used for selecting the subset of MSEs that can reliably be associated to stress redistribution processes. Section 4 describes the spatial location of the MSEs, based on an algorithm validated on artificial source events defined with known locations. The location magnitude of the MSEs is presented in Section 5 with a preliminary analogy with earthquake seismology. In Section 6, we assess the damage mechanisms associated with the recorded MSEs and discuss the over-all results in terms of *in situ* stress redistribution induced by the gallery excavation.

2 GEOLOGICAL AND EXPERIMENTAL CONTEXT

2.1 Geological formation and excavation operation

The Mont Terri Underground Rock Laboratory (URL) is a research facility located at a depth of 300 m below the surface in an argillaceous claystone (Opalinus Clay; Thury & Bossart 1999) allowing for *in situ* geophysical investigations to be carried out. In the URL (Fig. 1), the observed tectonic faults can be compiled into three main fault systems (Nussbaum *et al.* 2011): (i) moderately SSE-dipping reverse faults, (ii) low angle SW-dipping fault planes and flat-lying (sub-horizontal) faults, and (iii) moderately to steeply inclined N to NNE-striking sinistral strike-slip faults.

In 2008, an original gallery excavation method using a road header was tested in the URL. This technique allows for a smoother excavation that limits the extent of the induced damaged zone surrounding the final gallery (Bossart *et al.* 2004). The new gallery, called Ga08, was excavated to join the pre-existing end-face of an earlier gallery, called Ga04. The excavation operation was dedicated to the so-called EZ-G08 experiments which consisted in monitoring a fresh Excavation Damage Zone (EDZ). To do so, different geophysical methods have been developed for the *in situ* measurements, including electrical, self-potential and acoustic experiments (Nicollin *et al.* 2010; Maineult *et al.* 2013; Le Gonidec *et al.* 2012). The present paper deals with the acoustic experiments, installed in sub-horizontal boreholes (Fig. 2), which started on July 10 at 7:30 p.m., when the length of the rock mass segment was L = 8.6 m (excavation operations are then still going on in Ga08), and ended on July 23. The time schedule of the excavation operation is available from the excavation contractor, i.e. periods of activity/inactivity are well documented on an onboard journal with an estimated uncertainty of about 15 minutes. The excavation and lining of the upper part of Ga08 stopped on July 11 at noon, and the lower part of the gallery was finished excavating on July 12 at 6 p.m. Before this date, various excavation activities were intermittently going on at the Ga08 excavation front (Ga08 front-face). After this date, the rock mass segment was L = 8 m in length, with no excavation
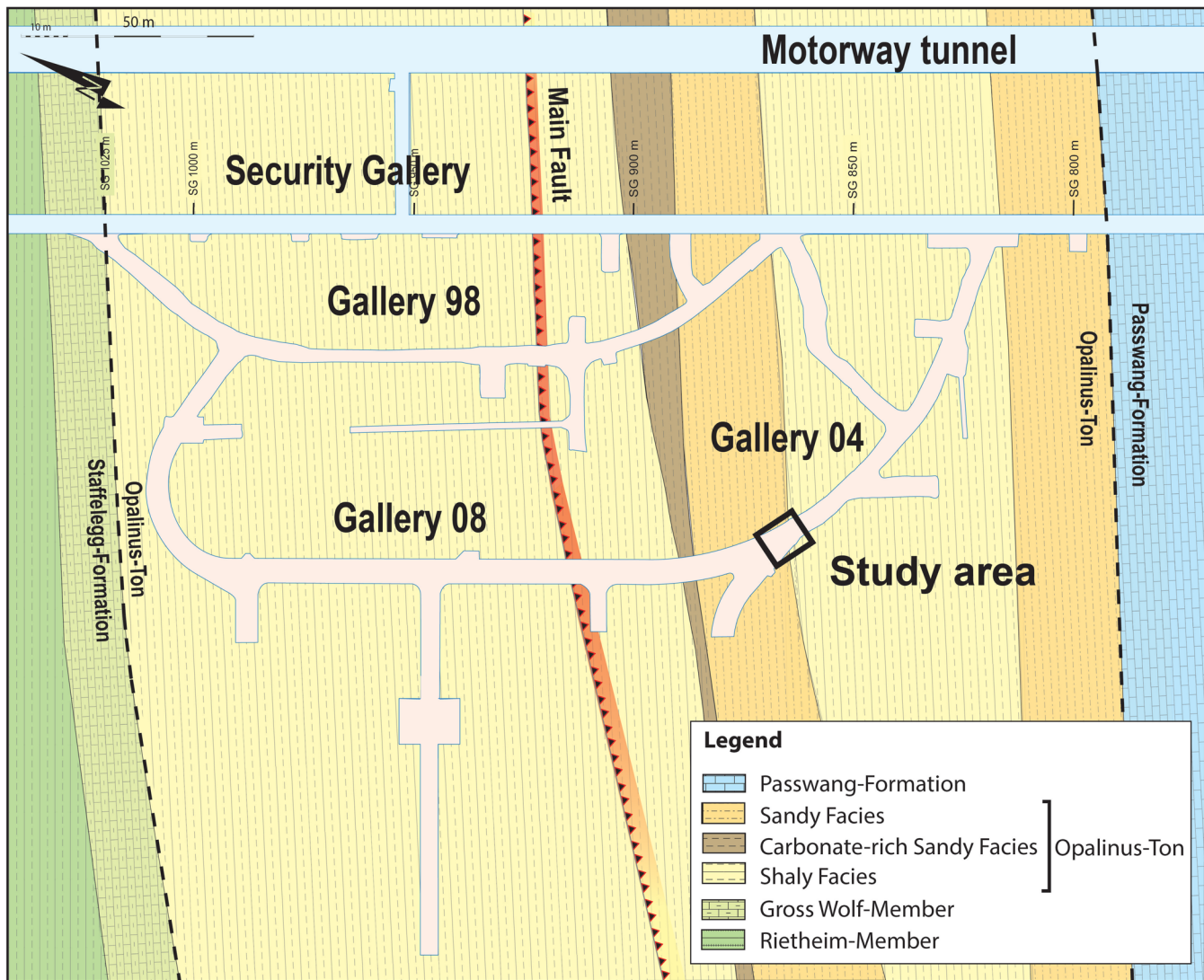
Figure 1. General view of geological map of the Mont Terri URL. The black box indicates the location of the so-called EZ-G08 experiments, at the junction between galleries Ga08 and Ga04 with the north and south sidewalls in a sandy and shaly facies, respectively.
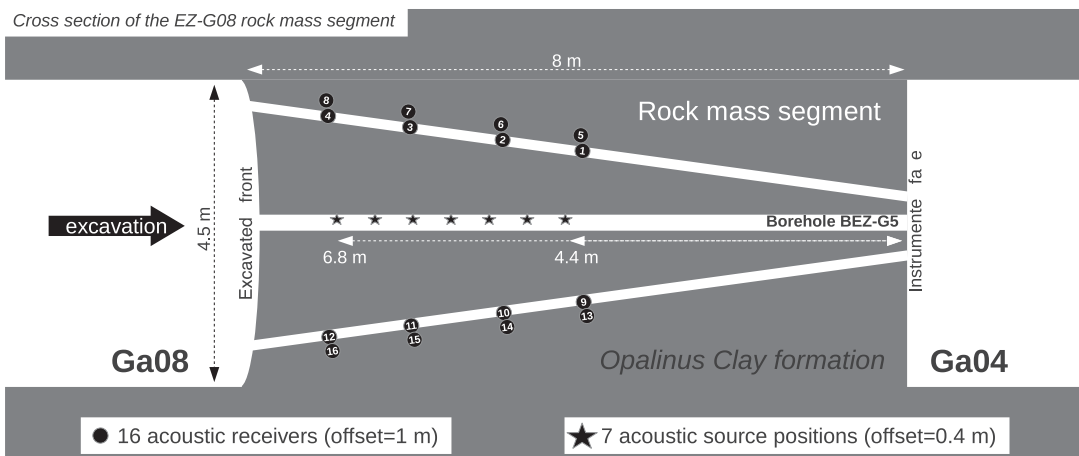
Figure 2. Schematic cross section of the rock mass segment (after 2008 July 12, 6 p.m.). The excavation operation cames from the left-hand side (gallery Ga08) and the opposite face (gallery Ga04) was instrumented for acoustic measurements. Ultrasonic measurements involve an active source that was introduced at different depths (black stars) in a central borehole (BEZ-G5). Sixteen acoustic receivers (black points) composed the acoustic arrays introduced in subhorizontal boreholes.

activity until the end of the measurement period (July 23). Most of the acoustic measurements took place during this period of time, in the general context illustrated in Fig. 2. Note that the gallery has an elliptical cross-section with an average diameter of 4.5 m, i.e. approximately half the length of the remaining rock mass segment.

The study area, mainly affected by the SSE-dipping reverse faults sub-parallel to the bedding planes, is located at the junction between two different geological facies (Fig. 1): a shaly facies, with argilla-ceous and marly shales, and a sandy facies, with sandstone layers and sandy limestone lenses in marly shales (Nussbaum *et al.* 2011).

2.2 Site instrumentation for the acoustic experiments

A full description of the site instrumentation and acoustic experi-ments designed and deployed for the EZ-G08 rock mass monitoring can be found in Le Gonidec *et al.* (2012), but a brief reminder of the main features is required to clearly understand the acoustic data analysis. An omnidirectional acoustic source was placed inside the borehole BEZ-G5 located at the center of the rock mass segment (Fig. 2). The source consisted in a piezo-electric transducer enclosed in a watertight balloon filled with pressurized oil to improve the me-chanical coupling with the borehole wall. The acoustic source, fixed to a long metal rod, was introduced inside BEZ-G5 and moved by hand at 7 different depths inside the borehole, from 4.4 to 6.8 m, nominally 0.4 m apart (black stars in Fig. 2). A fixed network of 16 acoustic receivers was located around BEZ-G5, divided into four linear arrays of 4 receivers each positioned 1 m apart (black dots in Fig. 2) along sub-horizontal boreholes (BEZ-G16 to BEZ-G19). The receivers were fixed on a holding pole and mounted using stiff springs in order to provide a good coupling between the spherical active face of the transducers and the cylindrical borehole wall.

At each position inside BEZ-G5, the acoustic source pulsed me-chanical vibrations into the rock mass segment, with a known cen-tral frequency, nominally ~30 kHz. The transmitted signals were recorded at each receiver of the acoustic network. The combina-tion of the acoustic source with an array of receivers allows for the assessment of the directional and time dependency of *P*-wave velocities, i.e. a so-called seismic survey was performed at regular time intervals during the experiment, nominally once a day. The traveltimes between each source position and each receiver was es-timated from the recorded waveforms. The corresponding *P*-wave velocities were calculated based on these flight times and known distances between each source position and each receiver, assum-ing that distances between source positions and receivers do not significantly change with time. The seismic surveys show a strong elastic anisotropy of the *P*-wave velocity wavefield with a mini-mum wave speed of 2750 m s^{-1} across the shale bedding planes, and a maximum wave speed of 3300 m s^{-1} along these planes (Le Gonidec *et al.* 2012). No significant changes in the velocity field with time was evidenced, possibly due to the uncertainty asso-ciated with the manual repositioning of the acoustic source within the borehole BEZ-G5.

Between two consecutive seismic surveys, the acoustic source was turned off and the acoustic network was used to detect and record spontaneous MSEs taking place in and around the rock mass segment during and after the excavation operations. In the following, we mainly focus on the microseismicity aspect of the experiment and use the velocity field reported in Le Gonidec *et al.* (2012) to locate the MSEs in space and time. Based on the average ambient noise level observed for each receiver prior to the start of the experiment, a specific threshold voltage was set for each of them (typically

50 mV) such that the amount of recorded data remains manageable. The recording trigger logic was set as follows: 'if a given number of receivers (typically 4) reaches the preset threshold within a given time-window (typically 1 ms), the system triggers and starts the acquisition of 2048 points at a sampling rate of 500 kHz on the acoustic receivers'. In order to record full event waveforms, 4096 μs in length, the first 25 per cent of these points consists in pre-trigger points. Note that among the 16 channels of the acoustic network, the first channel (No. 1) was set as the triggering channel and the others as recording channels (No. 2 to 16), i.e. each acoustic event is associated to 15 actual waveforms.

3 IDENTIFICATION OF MSEs AMONG THE RAW DATA SET OF EVENTS

By the end of this 14-d experiment, all events fulfilling the criteria described above, that is, based on a fixed threshold in mV (50) for a fixed number of triggered channels (4), were automatically recorded in the so-called raw data set of events. As a consequence, the raw data set includes ambient noises induced by the gallery being excavated, electronic noise and other artefacts, in addition to potential real microseismic events belonging to the so-called MSE catalogue.

3.1 Raw data set of events

During the acoustic experiments to monitor the rock mass segment before and after the excavation operations stopped, 56 446 events have been detected and recorded in the raw data set. The time history of these events is represented by the vertical black lines in Fig. 3(a) before the excavation has stopped and in Fig. 3(b) for the whole du-ration of the experiment. As mentioned above, the time schedule of the excavation operations is available, reported in blue in Fig. 3(a). We do not observe any correlation between the occurrence of the recorded events (black) and the excavation operations (blue). It turns out that the *a priori* criteria set for the detection/recording of the events are not well suited to high frequency data acquisition in a noisy gallery environment, where notable variations of the ambient noise level and perturbations of the electrical network occurs with-out much control on our side. For instance, many undesired events were triggered by electromagnetic disturbances, appearing as spikes simultaneously recorded on several receivers (Figs 4a and b). Other spurious events are related to waveforms electronically distorted during the recording process, characterized by a perfectly flat am-plitude at the beginning of the waveform (Fig. 4c) probably related to undetermined issue in the pre-triggering part of the recording. It is believed that these three types of spurious waveforms are due to cross talks between the triggering channel (No. 1) and the 15 recording channels (No. 2–16). Low S/N ratio waveforms recorded on a single receiver (Fig. 4d) are believed to be real, although weak, microseismic events, which could not be considered for an accu-rate determination of their spatial location or source mechanism as discussed in the following sections.

This highlights the first objective of the present paper, that is, the identification of the *a priori* weak MSEs buried in the rather large raw data set of 56 446 events. If MSEs do exist, when do they happen during the monitoring period and where are they located in the rock mass segment? In order to answer with confidence these two questions, we have to filter the raw data set and come up with a catalogue of actual MSEs, that is, to identify the true MSEs by removing the undesired events, in particular the ones belonging to one of the classes illustrated in Fig. 4.
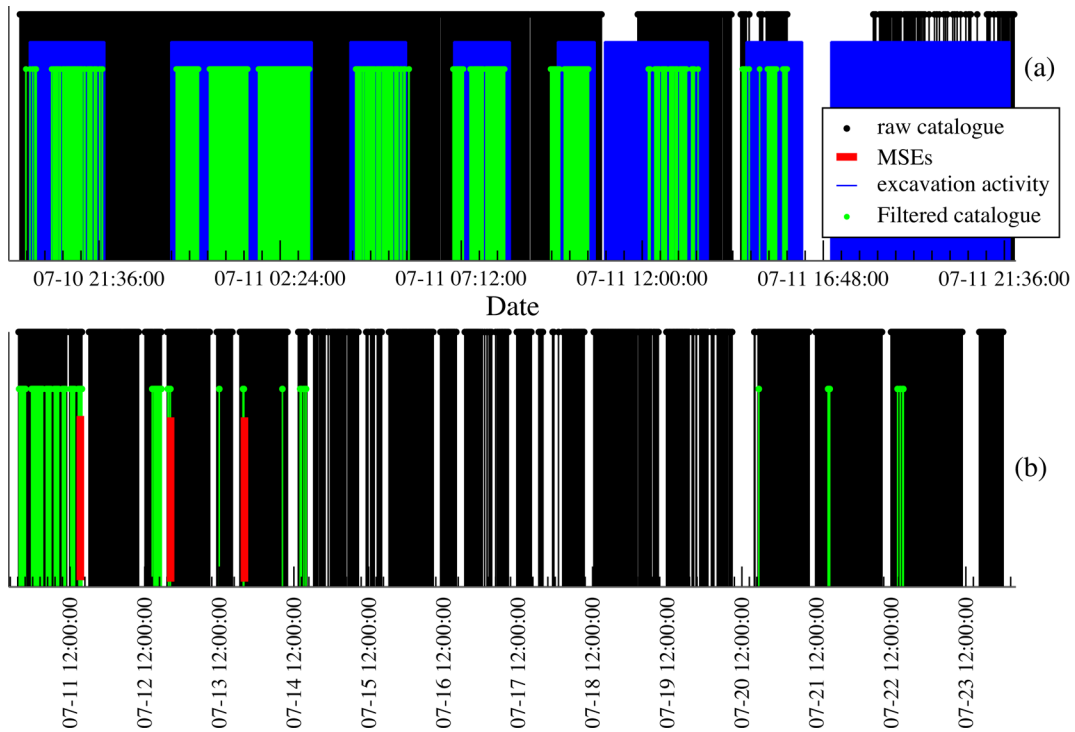
Figure 3. Time history of the 56 446 events of the raw data set (black lines) detailed for the period of excavation activity before July 12 (a) and for the whole period of experiment between July 10 and 23 (b). After the multistep filtering method, 20 per cent of the events are kept (green lines), in coherence with the time schedule of the excavation operation (blue zones). Finally, only 278 MSEs have been identified, located at three main time periods (red lines).
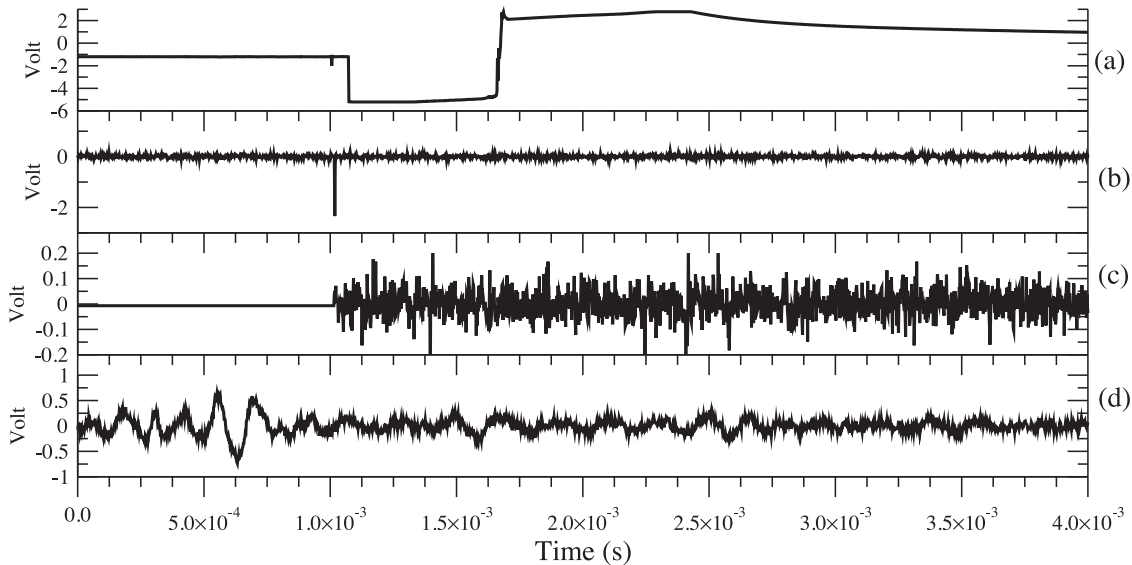
Figure 4. Illustrations of different recorded waveforms: (a, b and c) electronic artefacts and (d) low signal-to-noise ratio.

3.2 Catalogue of microseismic events

In this section, we present an efficient semi-automatic, yet reliable, method to select the actual MSEs among the raw data set of recorded events. Actually, this catalogue of MSEs results from the rejection of undesired events and is not exhaustive. For instance, the limited frequency band of the receivers does not allow for detection of potential MSEs with a frequency outside this band. In other words, weak events can be hidden in noisy waveforms (extremely low S/N ratio), or are so weak that they do not even trigger a detection/recording with the preset trigger logic. As a consequence, it is important to note that the filtered catalogue of microseismic events described below can not be considered as complete. The main criteria of the automatic multistep filtering algorithm are based on (i) the frequency content, (ii) S/N ratio of the associated waveforms and (iii) on the time history of the recorded events.

The first criterion for selecting MSEs among all recorded events is based on the frequency content. The acoustic receivers are characterized by a quasi-flat response in the frequency band 2 Hz–60 kHz. This frequency range is well suited to wave travel distances of few meters in a shale formation for which *P*-wave velocity is of the order of 3000 m s^{-1}. Higher frequencies would be too attenuated, and

lower frequencies would yield a wavelength too large in view of the propagation pathlength. The waveforms sampling frequency was set to 500 kHz to better estimate the *P*-waves arrival time. We consider a frequency lower band of 250 Hz, required to reliably identify and process a waveform recorded in a time window of 4096 μs. For the frequency upper bound, an inspection of the waveforms frequency spectrum shows no significant energy content at frequencies larger than 20 kHz, with an energy peak around 10 kHz. As a consequence, a zero-phase bandpass filter 200 Hz–20 kHz is first applied on the 15 waveforms of the 56 446 events. Note that this frequency range corresponds to audible events.

In a second step, we flag all waveforms which maximum amplitude is strongly affected by the previous frequency bandpass filter. This is particularly efficient to flag waveforms related to electronic noise, characterized by broadband spikes (Figs 4a and b), or to seismic surveys, involving source signals in the frequency range ∼30 kHz. We also flag the waveforms of weak S/N ratio, which can not be correctly processed in particular in terms of identification of the first arrival time. These criteria make the selection very restrictive, the benefit being a better identification of true MSEs and a more reliable processing of the selected events. As a first pass through this events filtering procedure, all events for which five waveforms ore more are flagged are rejected. According to this restrictive filtering, most of the events in the raw data set are discarded, that is, less than 20 per cent of the whole set of events can be considered as potential MSEs. Actually, the time history of the remaining events is represented by vertical green lines in Fig. 3.

The last step involves the time schedule of the excavation operations, which periods of activity are represented in blue in Fig. 3(a). An obvious correlation, that does not exist with the occurrence of the raw data set events (black) noted in Section 3.1, is highlighted between the excavation activity and the occurrence of the events (green) that remain from the previous steps of the filtering

algorithm. This clearly demonstrates *a posteriori* the effectiveness of the filtering/selection protocol used above, and shows that excavation operations until July 12 at 6 p.m. are also responsible for part of the 20 per cent remaining events. After this date, the time schedule of the excavation operations indicates two main activities: on July 14 and 22, punctual coring/sampling operations were carried out for research purposes and are responsible for acoustic events further detailed later in the text. Finally, we handily checked the remaining events to assess the selection reliability. The few events (10) located on July 20 and 21 could be manually identified as noise and filtered out with confidence. The events located on July 12 and 13 are characterized by high quality waveforms and do not correspond to any excavation activity: they are thus identified as actual MSEs. On July 11, during the excavation operations, hundreds of consecutive events are recorded with very similar waveforms, equivalent to a burst of actual MSEs.

As a key result, the MSE catalogue is actually structured in three main periods of time. The first period occurs on July 11 between 2:39 p.m. and 2:50 p.m., that is, during excavation operations, where hundreds of consecutive events (burst) are recorded with very similar waveforms. Among them, only 191 MSEs can effectively be spatially relocated based on the identification of the first arrival time as discussed in Section 4. The other events recorded during this burst are discarded. The two other periods occur after the excavation operations have stopped: on July 12, 71 MSEs have been detected between 7:28 p.m. and 8:18 p.m., and on July 13, 16 MSEs have been detected at 7:39 p.m. The 15 raw waveforms (No. 2–16) constituting a single MSE recorded on July 12 are illustrated in Fig. 5(a): the event belongs to the MSE catalogue because only two waveforms have been rejected (No. 2 and 8) according to the filtering protocol detailed above, and the remaining waveforms are of sufficient quality to permit first arrival time picking and subsequent event spatial relocation. Finally, 278 MSEs events are considered as
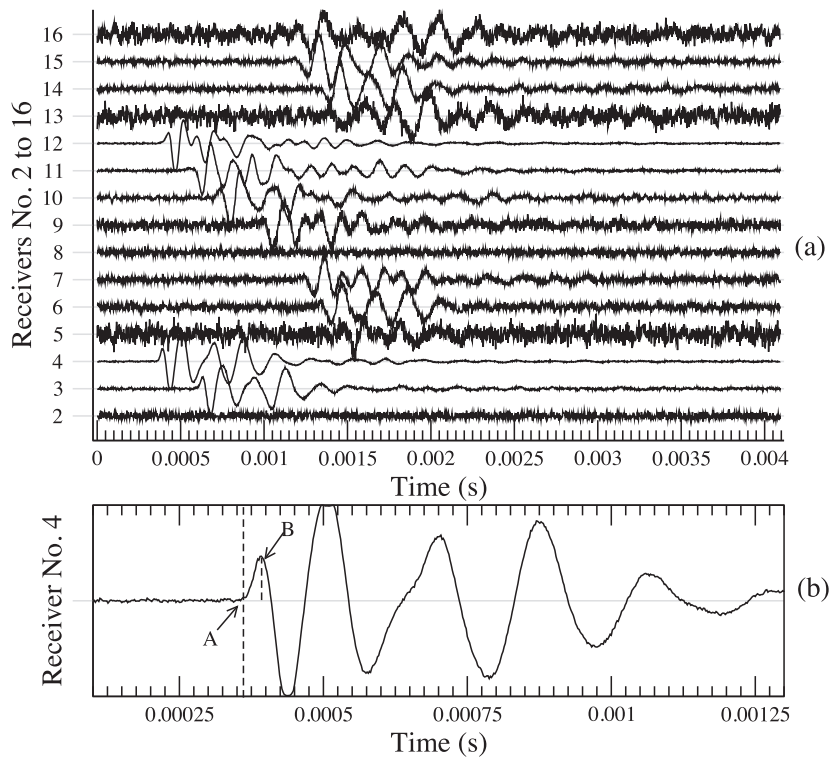
Figure 5. (a) Illustration of the 15 raw waveforms of an event belonging to the MSE catalogue (normalized amplitudes). (b) Details of the waveform recorded on channel No. 4: the arrows A and B point towards the arrival time and amplitude of the first movement, respectively.

Table 1. Identified microseismic events.

Date	Number of located MSEs	Number of failure mechanisms	Time
July 11	191	–	2:39–2:50 p.m.
July 12	71	50	7:28–8:18 p.m.
July 13	16	11	7:39 p.m.

real (Table 1) associated with damage processes around the freshly excavated gallery. The spatial location of these MSEs is detailed in the following.

4 SPATIAL LOCATION OF THE MICROSEISMIC EVENTS

In the preliminary analysis of the EZ-G08 experiment reported in Le Gonidec *et al.* (2012), the detection and spatial location of more than 2000 acoustic events have been carried out using the so-called Collapsing Grid Search routine (Pettitt *et al.* 2003), implemented in the Insite® Seimic Processor software (Applied Seismology Consultants, ASC Ltd.). However, no selection of the events was carried out and no estimation of the uncertainty associated with their spatial location was provided. In this study, a comprehensive analysis of the events, restricted to the 278 real MSEs, and their attributes are reported along with uncertainty estimates.

4.1 Procedure and accuracy of the spatial location from known anthropic acoustic sources

As part of the EZ-G08 experiments, *P*-wave velocity surveys were performed between an active acoustic source, located at different depths in the borehole BEZ-G5, and the array of receivers surrounding it (Fig. 2). These measurements allowed determining the transversely isotropic *P*-wave velocity model (Le Gonidec *et al.* 2012). In addition, the acoustic source can also be used as an artificial acoustic event that can be treated as any other event belonging to the MSE catalogue, and therefore be spatially located using the

same algorithm and velocity model. The advantage of such artificial events over the MSEs is that their positions in space are known at all times: seven source positions were ranging between 4.4 and 6.8 m deep inside BEZ-G5. For each position between 4.4 and 6.4 m, more than 70 seismic surveys have been performed during the experiments. For the last 6.8 m position, only four measurements were available because BEZ-G5 eventually collapsed and did not allow introducing the acoustic source up to that particular position (Le Gonidec *et al.* 2012). In total, 453 artificial ultrasonic events could finally be located according to a method that will be applied to the actual MSEs. This approach allows us to assess the reliability and accuracy of the spatial location procedure as a whole, that is, velocity model, flight time picking and convergence of the inversion algorithm.

The source location is an inverse procedure which consists in minimizing the difference between two source–receiver traveltimes: one is measured in the experiment and the other is calculated with the velocity model of the medium. The former is picked on the recorded waveform (see Fig. 5b, arrow A), and the latter involves the transversely isotropic *P*-wave velocity field reported in Le Gonidec *et al.* (2012). The minimization is performed simultaneously on all receivers for a given source (MSE). The location error is determined from the sum of the traveltime residuals between the source and each receiver of the acoustic array. In this work, the error-minimization is performed via the Simplex iterative algorithm implemented within Insite® software package (ASC Ltd.), based on the Downhill Simplex Method (Nelder & Mead 1965; Press *et al.* 1994). A restrictive condition is used to increase the location confidence. It consists in allowing the algorithm to proceed only if the quality of at least six over the 15 recorded waveforms is good enough to confidently identify the traveltime.

The results of the spatial location of the 453 artificial (emitters) events are displayed in a geographical west/north reference in Fig. 6(a). In order to assess the quality of the spatial locations obtained in this manner, the results are displayed relative to the known position of the borehole BEZ-G5 in side (Fig. 6b), top (Fig. 6c) and front (Fig. 6d) views. The black circles represent the end-face
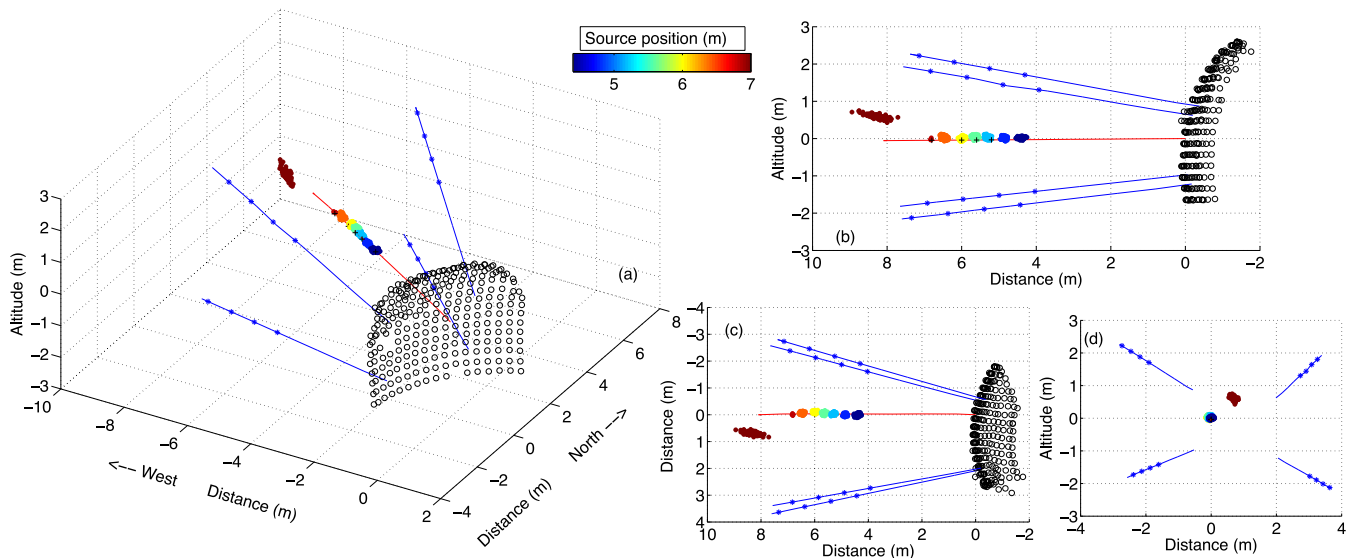
Figure 6. (a) Spatial location of 453 ultrasonic sources of acoustic surveys (source depths location in colours) viewed from the Ga04 end-face (black circles) in the west/north reference. (b–d) Spatial locations relative to the borehole BEZ-G5 orientation with a side, top and Ga08 front views, respectively. Blue lines represent the subhorizontal boreholes for the four acoustic arrays with the positions of the transducers (blue stars). The red line represents BEZ-G5 where the black crosses locate the seven source positions (some can be hidden by the data).
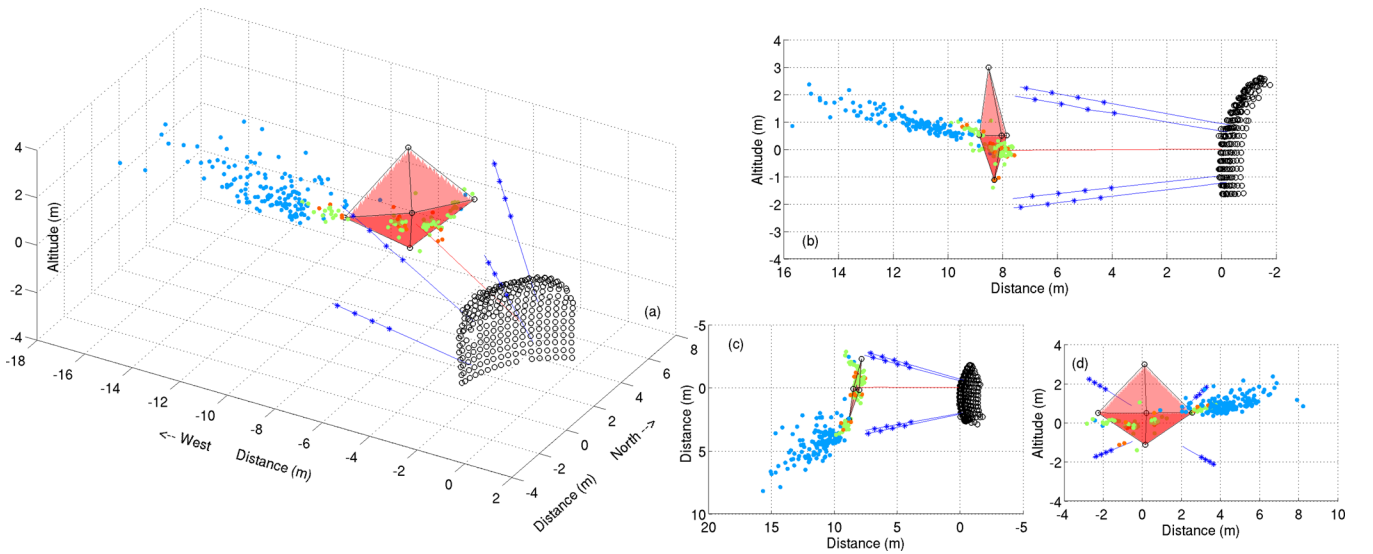
Figure 7. (a) Spatial location of the sources of the 278 microseismic events (July 11, 12 and 13 in blue, green and red, respectively) viewed from the Ga04 end-face (black circles) in the west/north reference. The position of the end-face of Ga8 is identified by the red tetrahedral surface. (b–d) Spatial locations relative to the borehole BEZ-G5 orientation with a side, top and Ga08 front views, respectively. Blue lines represent the subhorizontal boreholes for the 16 acoustic receivers (blue stars). The red line represents the BEZ-G5 borehole.

of gallery Ga04 as modeled from a multipoint topographic mapping performed prior the start of the experiment. Each of the seven coloured clusters of dots (dark blue to red) corresponds to the location of the artificial events recorded for a given position of the acoustic source for various surveys conducted during the course of the experiment and using the devised transversely isotropic velocity model. It can be seen that each cluster matches well with the known nominal positions of the source (indicated by black crosses along the red line representing the BEZ-G5 borehole). In particular, the seven clusters are very well located along the borehole axis in Fig. 6(d). The estimated uncertainty in the spatial location of the source positions amounts to about 20 cm around the nominal source positions inside the rock mass segment of 8 m in length. This uncertainty estimate represents the average distance from the located artificial sources (coloured dots) to their theoretical positions (black crosses). This assessment proves the validity and accuracy of the spatial location of artificial source events, especially in terms of the velocity model used.

Prior to applying this location procedure to actual MSEs, it has also been tested against another set of artificial events associated with a drilling operation. On July 14, an extra borehole was drilled on the newly excavated end-face of the gallery Ga08. A total of 70 events associated with this operation were recorded and located, yielding a good match with the known borehole position and orientation (cluster of brown dots in Fig. 6). This assessment proves that the spatial location procedure developed here performs well, not only on artificial source events but also on acoustic events associated with a borehole drilling. This location procedure is therefore confidently applied to actual MSEs.

4.2 Spatial distribution of the microseismic sources

Following the method developed above, the 278 recorded and selected MSEs were spatially located. The results are plotted in Fig. 7. In this figure, the red tetrahedral surface stands for the Ga08 front-face, as modeled from the five points available from a topographic mapping performed after the excavation operation stopped. The black circles represent the Ga04 end-face and the source borehole

BEZ-G5 (red line) crosses the whole rock mass segment under study, joining the two faces of Ga04 and Ga08, respectively. The MSE events (dots) are coloured according to the day they occurred.

In blue, the burst of events detected on July 11 seems to be contained in an apparent plane located within the sidewall of Ga08, on the right-hand side when facing the Ga08 front-face (blue dots in Fig. 7). However, the apparent plane does not fit with any particular pre-existing geological structure observed on site. The results put in evidence an asymmetrical distribution of the sources of the MSEs around the Ga08 front-face: the events detected on July 11 cluster in the right-hand side close to the shaly facies, and none is identified in the sandy left-hand side (Fig. 1).

The green and red dots represent the MSEs recorded on July 12 and on July 13, and both cluster on similar zones located around the Ga08 front-face (green and red dots in Fig. 7, respectively). With the accuracy of the location procedure (roughly 20 cm), the sources of these MSEs can be divided into two main clusters. The first cluster includes the MSEs located in the right-hand sidewall of the excavation front. The second cluster corresponds to the MSEs located ahead the excavation front, that is, mainly at the free surface of the rock mass.

5 LOCATION MAGNITUDE OF THE MICROSEISMIC SOURCES

In order to estimate the amount of energy radiated by a given MSE, a simple approach consists in quantifying the event magnitude based on the energy carried by the associated waveforms recorded by the array of acoustic receivers. As a first approximation, the location magnitude M_j of the event j can be described by (Pettitt *et al.* 2003):

$$M_j = \log\left(\frac{1}{n}\sum_{i=1}^{i=n} W_i^{\mathrm{rms}}.d_i\right), \tag{1}$$

where n is the number of triggered receivers, W_i^{rms} the rms amplitude of the waveform recorded at receiver i located at a distance d_i from the event j. The last parameter implies that the spatial location of event j is known. The implicit assumptions underlying this estimate
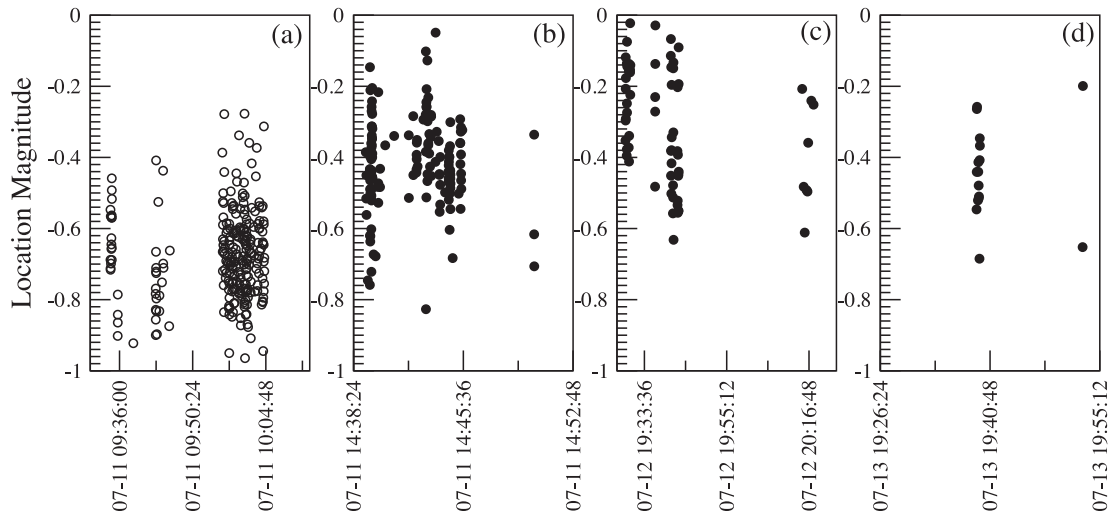
Figure 8. (a) Location magnitude of acoustic events associated to the excavation activity (250 events). (b) Location magnitude of the burst of acoustic events recorded on July 11 (191 events). (c) and (d) Location magnitude of the microseismic events recorded on July 12 (71 MSEs) and 13 (16 MSEs), respectively.

of the radiated energy are: (i) the energy radiation pattern of an event is spatially uniform (far field approximation in a scattering medium), (ii) the mechanical coupling of all receivers to the rock surface is similar and (iii) the intrinsic response (acceleration-to-voltage characteristic) of all receivers is similar. The location magnitude can then be assessed for each of the 278 MSEs. However, since the receivers are not calibrated (unknown voltage-to-acceleration), M_j remains effectively a voltage, used as a proxy for the amount of mechanical energy radiated by the MSEs.

For comparison purposes, the location magnitude of the acoustic events induced by the road header excavation operation are also displayed (black circles in Fig. 8a): their average location magnitude is about -0.7. The location magnitude of the 278 MSEs are plotted versus time of occurrence in Figs 8(b)–(d) (black dots). The burst of MSEs identified on July 11 shows a higher average magnitude, close to -0.4 (Fig. 8b). On July 12, the average magnitude is even higher, near -0.3, with representative magnitudes up to -0.1 (Fig. 8c), and decreases to -0.4 for the MSEs recorded on July 13 (Fig. 8d). It is interesting to note the temporal variation of the estimated magnitude of the MSEs, with a peak observed on July 12 and a subsequent decrease the following day.

A natural extension of this quantitative analysis consists in estimating the number N of MSEs which magnitudes are higher or equal to M, that is, a method traditionally reported in earthquake seismology which consists in fitting the frequency–magnitude distribution with a power law (Gutenberg & Richter 1944): $\log(N) = a - bM$, where a and b are positive constant values. The b-value is generally close to 1 in seismogenic regions, but can reach 2.5 or more during an earthquake swarm, that is, an earthquake activity clustered in space an time with a large amount of small events (Kayal 2008). As a preliminary approach, an analogue estimation of the b-value is performed here for the MSEs induced by the gallery excavation. Because of the limited sensitivity of the available receivers, magnitudes $M < -0.6$ are not considered. A value of $b = 2.8$ is obtained for this experiment, that is, a value comparable to the b-value of earthquake swarms (Kayal 2008). This suggests that the stress redistribution occurring around the excavated gallery in this region of the Opalinus Clay formation are of sufficient amplitude to induce a swarm of MSEs similar in nature to swarms observed for earthquakes occurring at much larger scales.

6 SPATIAL DISTRIBUTION OF DAMAGE MECHANISMS

In this section, we assess the damage mechanism associated with recorded MSEs. This processing requires not only a reliable identification of the first arrival time but also the amplitude of the first movement in the recorded waveforms (see Fig. 5b, arrows A and B, respectively), which in turn requires good quality waveforms. Such conditions are satisfied for only 61 MSEs among the 278 located MSEs: 50 on July 12 and 11 on July 13. The quality of the MSEs recorded on July 11 is unfortunately not sufficient.

The source mechanisms associated with the 61 selected MSEs are determined using a time-domain Moment Tensor (MT) approach (Pettitt 1998; Young *et al.* 2000). The MT inversion is based on the P-wave first motions as seen on waveforms with reasonable S/N ratio. This approach involves knowledge of first P-wave arrival time (see Fig. 5b, arrow A), (relative) amplitude and polarization (arrow B) at each receiver sensing a given event. This is not a simple task, in particular in a soft rock as the Opalinus clay where the waveform quality is often limited.

To assess the source mechanisms, we use the inversion algorithm implemented in the Insite® software (ASC Ltd.). This approach is based on several assumptions: a point source, a delta type source–time function, a far-field radiation pattern, and a homogeneous and isotropic medium in which the radiation propagates. The two last assumptions are obviously not strictly consistent with the observations reported earlier in the manuscript and in Le Gonidec *et al.* (2012), that is, the Opalinus Clay in this region is rather transversely isotropic with an inclined symmetry plane, and *a priori* likely to be heterogeneous (although this last point is difficult to assess with the available data). Yet, as a first order approximation in the following analysis, the mean P-wave velocity of the shale in this region is used, that is, $3000\,\mathrm{m\,s^{-1}}$. An approximate frequency of $10\,\mathrm{kHz}$ for the MSEs can also be used, corresponding to an approximate wavelength of $30\,\mathrm{cm}$, that is, the far-field assumption is approximately fulfilled in view of the dimensions of the rock segment investigated and the size of the array of receivers. Another input of the inversion algorithm is the quality factor $Q \propto 1/\alpha$ of the propagation medium (Jones 1995), where α (Np/m) is the absorption coefficient in the amplitude $A = A_0 e^{-\alpha(r-r_0)}$ of the decaying plane wave at the

location r, with A_0 the amplitude at the initial location r_0:

$$Q = \frac{\pi(r - r_0)}{\lambda \ln\left(\frac{A_0 r_0}{Ar}\right)}, \tag{2}$$

where λ is the acoustic wavelength. An order of magnitude for Q can be estimated from the active monitoring part of the experiment (seismic surveys). A value $Q \simeq 20$ is found, which corresponds to a strongly attenuating medium, consistent with sedimentary rocks (Jones 1995). The quality of a source mechanism inversion can be estimated from the amplitude residuals $A_R \in [0; 2]$ that is the difference between the measured and calculated amplitudes (Pettitt *et al.* 2003).

According to the method described above, we perform the source mechanism inversion on only 61 out of the 278 recorded and selected MSEs. In average, the amplitude residual of the inversions is $A_R = 0.13$ and the standard deviation is 0.07, consistent with a reliable inversion procedure (Pettitt *et al.* 2003). But let us recall that the analysis of the source mechanisms relies on many assumptions that are probably not strictly fulfilled. However, within these given limitations, the aim here is to assess if the two clusters of MSEs identified on July 12 and July 13 correspond to similar or contrasting damage mechanisms in relation to the stress redistribution process in the shale formation.

The source type diagram initially introduced by Hudson *et al.* (1989), also called T–k plane, is used to plot the identified source mechanisms in an equal-area graph (Fig. 9a). The horizontal T-axis represents the magnitude of the deviatoric (shear) portion of the mechanism, while the vertical k-axis translates the magnitude of the isotropic (volumetric) part. In particular, dilatation (ISO), double-couple (DC) and compensated linear vector dipole (CLVD) mechanisms are characterized by $(T, k) = (0, 1)$, $(T, k) =$

$(0, 0)$ and $(T, k) = (-1, 0)$, respectively [see Fig. 9(b) for a geometrical illustration of the mechanisms proposed by Šílený & Milev (2008)]. The results of the inversion of the 61 MSEs are plotted in Fig. 9(a) where the source mechanism identified for each MSE is represented by a red ellipse. The geometric centre of the ellipse corresponds to the nominal source mechanism obtained through the inversion procedure, and its size relates to the inherent uncertainty (error) associated with the inversion. These errors are mainly related to the uncertainty in the picking of the *P*-wave first motion and associated amplitude determination. This is in turn related to the quality of the recorded waveforms, that is, the S/N ratio. Despite the scatter observed in Fig. 9(a), most of the identified source mechanisms tend to cluster around particular modes characterized by shear and opening components ($T < 0$ and $k > 0$). Fewer MSEs display shear and closure components ($T > 0$ and $k < 0$).

Since each identified source mechanism is effectively a mixture of ISO, DC and CLVD components, this information can be converted into a RGB colour scale for spatial representation purposes. Each MSE with known proportions of ISO, DC and CLVD is represented in Figs 10(a)–(d) by a point located in space with corresponding proportions of red, green and blue colours, respectively. It is obvious that the colour distribution (translating source types) is not random and two clusters can effectively be identified. For the first cluster, CLVD-dominated mechanisms (blue) are mostly located on the sidewall of the gallery, to the right-hand side when facing the excavation front. For the second cluster, DC-dominated mechanisms (green) are mostly located ahead the excavation front. This representation of the results clearly supports the existence of a correlation between the three main attributes of the recorded MSEs identified so far, which relate back to the stress redistribution processes taking place: spatial, temporal and damage mechanism attributes.
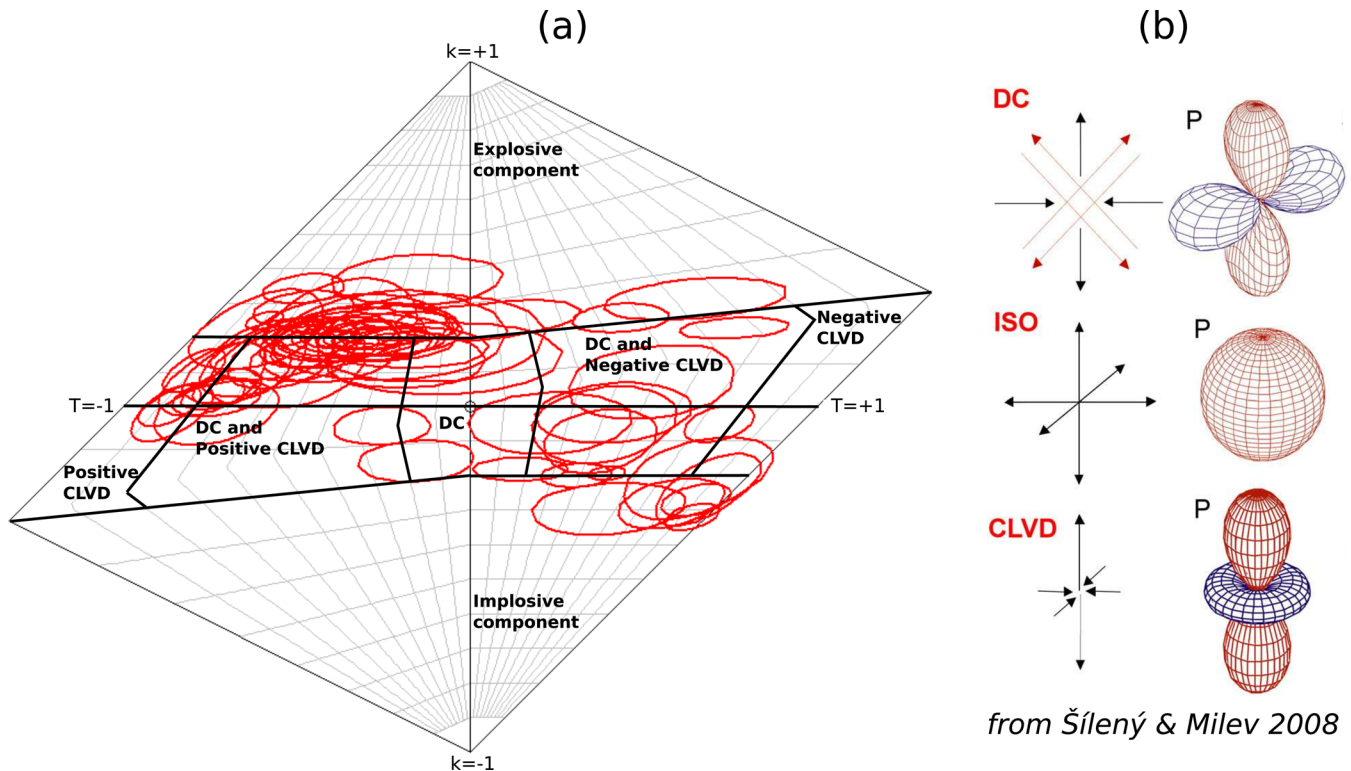
Figure 9. (a) Source mechanisms of the fully processed waveforms of 61 MSEs plotted in a Hudson $T - k$ plot with the red error ellipses related to the Moment Tensor inversion accuracy (average amplitude residual and standard deviation of the inversion operation: 0.13 and 0.07, respectively). The bold lines delimit the areas defined by Forney (1999). (b) Illustrations of the ISO, DC and CLVD mechanisms (modified from Šílený & Milev 2008).
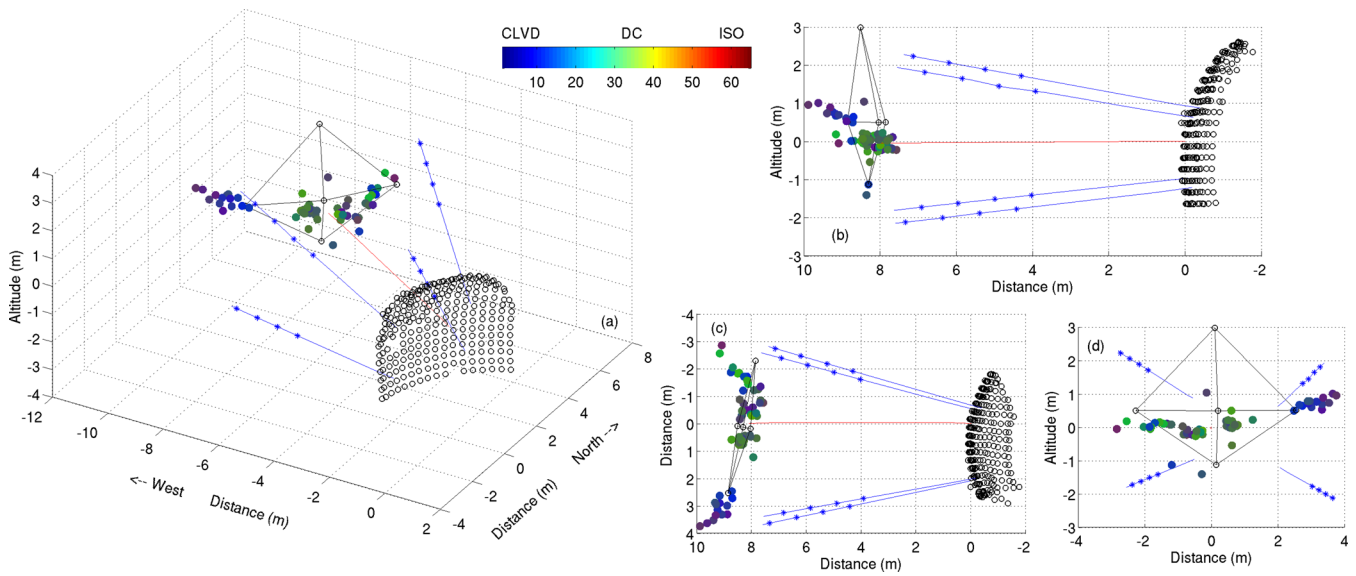
Figure 10. Source mechanisms of 61 microseismic events in RGB colours standing for isotropic (red), double-couple DC (green) and compensated linear vector dipole CLVD (blue). (a) Spatial distribution viewed from the Ga04 end-face (black circles) in the west/north reference. The position of the end-face of Ga8 is identified by the black tetrahedral feature. (b–d) Spatial distribution relative to the borehole BEZ-G5 orientation with a side, top and Ga08 front views, respectively. Blue lines represent the sub-horizontal boreholes for the 16 acoustic receivers (blue stars). The red line represents BEZ-G5.

7 DISCUSSION: IMPLICATION FOR THE EDZ

In addition to the choice of the excavation technique, many factors could influence the development and the geometry of an EDZ, as described by Blümling *et al.* (2007): (i) the lithology, (ii) the orientation of the gallery given the stress field anisotropy and orientation of the principal axes, (iii) the bedding planes (contributive to anisotropy and weakness planes) and tectonic fractures orientation with respect to the stress field, (iv) the anisotropy of the stress field in the vicinity of the gallery and (v) the mechanical properties and behaviour of the surrounding rock (e.g. compressive strength).

This work suggests that microseismic activity related to stress-redistribution is limited in both space and time (Fig. 7), in accordance with previous observations by Forney (1999) in the shaly facies sidewall during the excavation of the north part of the gallery 98 (north side of the Main fault, Fig. 1). Indeed, two subsets of MSEs are identified during the Ga08 mine-by test. The first one, a burst of 191 MSEs detected on July 11, is localized in the shaly facies of the southern sidewall of the gallery (blue dots in Fig. 7).

Unfortunately, no damage mechanism could be identified for these MSEs. The second one, composed of 87 MSEs detected the two following days (July 12 and 13), is localized in two main areas: on the right-hand side (south sidewall corner) of the excavation front and ahead the excavation front (green and red dots in Fig. 7). At these two locations, damage mechanisms based on the moment tensor inversion could be assessed with confidence (Fig. 10) and showed a dominant CLVD and DC component, respectively. The highest radiated energy was observed for the MSEs occurring on July 12 (Fig. 8), which must be related to larger sources and/or brutal damage mechanisms. These *in situ* results are in agreement with laboratory compression tests performed on centimetric samples where a brutal macroscopic failure phase exhibits intense AE activity, localized in space and time (Amann *et al.* 2012) and is associated with the highest radiated energy (e.g. Lockner *et al.* 1991; Amitrano 2003; Wassermann *et al.* 2009).

The different source-mechanism types may be explained by the direction of the Ga08 excavation with respect to the pre-existing geological features and the orientation of the stress field. Fig. 11 depicts a conceptual model of the stress pattern around the
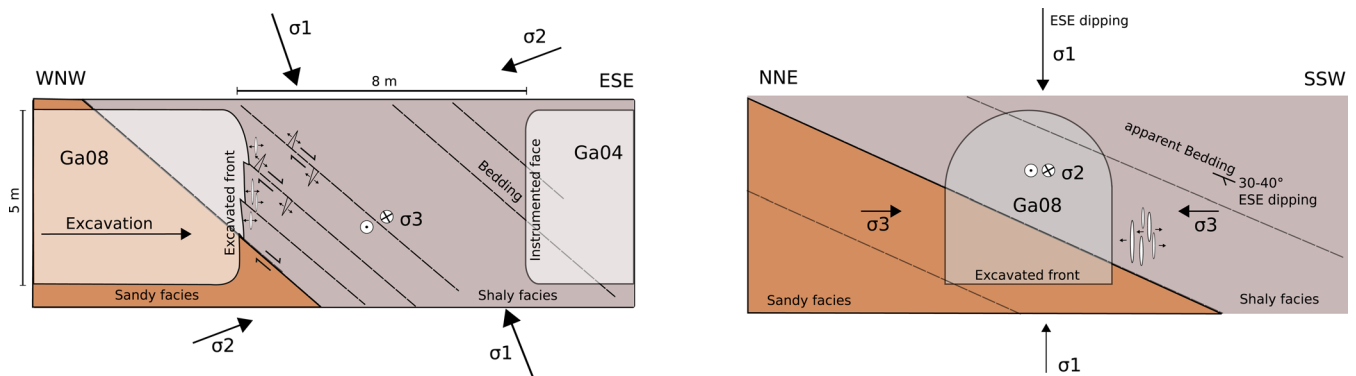
Figure 11. Conceptual representation of the stress pattern around an underground gallery excavated in a rock formation where the undisturbed maximum principal stress σ_1 is subvertical and compressive: (a) Side view from shaly facies sidewall (modified from Nussbaum *et al.* 2011) and (b) View from Ga08 in the direction of the excavation front.

excavation. At the Ga08 front-face, the bedding and subparallel faults, which dip with an angle of 45°, are free to slip because the excavation releases the boundary constraints at the front (reactivation of such features, and mainly bedding-parallel faults, is a common consequence of excavation operations). The dominant DC component highlighted for the MSEs detected at the freshly excavated front is in accordance with the shear fracture mode expected for slipage of such pre-existing structures. As a consequence of the shear movement along the pre-existing fault planes, wing cracks are expected to develop.

At the corner of the Ga08 front-face, bedding and sub-parallel faults are not free to slip because the excavation direction is nearly perpendicular to the bedding strike and does not induce any free boundary allowing the features to slip. Since the maximum compressive stress is subvertical in the Mont Terri URL (Fig. 11), tensile fractures may develop vertically as a consequence of axial splitting and may constitute the first phase of extensive cracking (vertical tensile cracks and fractures), that is, the so-called spalling features that develop around the gallery (Blümling *et al.* 2007) with an initiation process described by Martin (1997). Also observed in crystalline rocks (such as granites; Martin (1997)), spalling is clearly related to intense microseismic activity (Cai *et al.* 2001). Accordingly, the source mechanism of the MSEs detected at the Ga08 corner in the present study is a dominant CLVD component mechanism (Fig. 9 and Fig. 10), that is, a tensile fracturing already observed in many other field experiments (Martin *et al.* 2004; Blümling *et al.* 2007). This extensive cracking is also consistent with both the orientation of the Ga08 gallery, the geological features (bedding and faults planes), and the field observations, in particular the difference in lithology between the sandy and the shaly facies of the north and south sidewalls, respectively (Fig. 11). Note that the sidewall in the sandy facies is free of microseismic activity, that is, the EDZ distribution appears asymmetrical and controlled by the lithology of the excavated formations, in accordance with Blümling *et al.* (2007). Indeed, the stress threshold of crack initiation for the shaly facies (comprised between 2.5 and 4.3 MPa at low confining stress; Amann *et al.* 2012) is lower than that of the stiffer sandy facies, explaining the asymmetric geometry of the EDZ around the Ga08 front-face.

As a conclusion, the MSEs fault plane solution seems to be controlled by four major factors: the lithology, the geometry of the geological features, the gallery orientation and the direction of the main compressive stress.

8 CONCLUDING REMARKS

The purpose of the present work was to better understand the EDZ initiation processes and short-term evolution during the excavation of an underground gallery in a shaly formation such as the Opalinus (OPA) clay. In addition to electronic noise and artifacts recorded during the monitoring of the excavation, many acoustic activities are induced by the excavation operation, including cracking and crushing of the rock directly in contact with the excavating tools, noisy anthropic activities, and actual MSEs induced by stress redistribution around the gallery. Indeed, more than fifty thousands events have been recorded by the multichannel acoustic monitoring system. After a multi-step, multicriteria filtering process of the events, based on the frequency content of the events, the source location analysis, and the time schedule of the excavation operation, less than three hundred events are identified as true MSEs. A burst of MSEs is highlighted in the shaly facies sidewall of the gallery but unfortunately,

the associated source mechanisms could not be determined due to the low S/N ratio of the recorded waveforms. A second cluster of few tens of MSEs occurs in the two following days after the excavation operations are stopped. Some of them locate in the mid part of the shaly facies sidewall of the front-face, where the CLVD component of source mechanisms dominates: this suggests an axial splitting, a possible zone of initiation of spalling damage (Blümling *et al.* 2007; Yong *et al.* 2010) where extensive cracks nucleate and coalesce parallel to the major principal stress axis (Jaeger & Cook 1979). The others locate in the vicinity of the excavation front, characterized by a source mechanism with a dominant DC component: this mechanism can be attributed to shear process occurring preferentially along weakness planes such as bedding planes which direction and dip with respect to the stress field favour bedding plane reworking (see Fig. 11). Shear fracture or reworking can be associated locally to extensive cracks, as suggested in Fig. 11, and observed in damaged sidewall in Mont Terri by Nussbaum *et al.* (2011). No MSE is detected in the sandy facies of the opposite sidewall. Hence, the EDZ develops in a particularly complex zone, in terms of lithology and geometry, with two OPA clay facies—sandy and shaly—both anisotropic and with contrasting mechanical properties, involving dipping bedding planes. In addition, the perturbation of the stress field is also complex, most probably involving increase, decrease and rotation of the stress around the opening (Martin 1997).

The results of the Ga08 mine-by test experiments, consistent with previously published observations in crystalline rocks, clearly contribute to filling the gap for clayey formations. This study highlights different key points to discuss further. Is the EDZ around gallery Ga08 really asymetric or is our instrumentation unable to capture MSEs due to frequency or energy (S/N ratio, attenuation) limitations? Is the extensive damage only develop inside the shaly facies and only in the mid part of the corresponding sidewall? An accurate detection of the damage features is of particular importance because of its negative impact on the permeability of the surrounding rock (Souley *et al.* 2001; Bossart *et al.* 2002) and thus on the confining properties of a geological barrier. Mechanical modeling of the obviously complex loading path, taking into account the anisotropy and mechanical behaviour of the different facies (sandy and shaly) of the Opalinus Clay formation, is the next step to analyse the EDZ initiation and evolution in the context of the Ga08 mine-by test.

REFERENCES

Amann, F., Kaiser, P. & Button, E.A., 2012. Experimental study of brittle behavior of clay shale in rapid triaxial compression, *Rock Mech. Rock Eng.,* **45,** 21–33.

Amitrano, D., 2003. Brittleductile transition and associated seismicity: experimental and numerical studies and relationship with the b value, *J. geophys. Res.,* **108,** 2044, doi:10.1029/2001JB000680.

Baker, C. & Young, R.P., 1997. Evidence for extensile crack initiation in point source time-dependent moment tensor solutions, *Bull. seism. Soc. Am.,* **87,** 1442–1453.

Bastiaens, W., Bernier, F. & Li, X.L., 2007. SELFRAC: experiments and conclusions on fracturing, self-healing and self-sealing processes in clays, *Phys. Chem. Earth*, *Parts A/B/C*, **32,** 600–615.

Blümling, P., Bernier, F., Lebon, P. & Derek Martin, C., 2007. The excavation damaged zone in clay formations time-dependent behaviour and influence on performance assessment, *Phys. Chem. Earth*, *Parts A/B/C*, **32,** 588–599.

Bossart, P., Meier, P.M., Moeri, A., Trick, T. & Mayor, J.C., 2002. Geological and hydraulic characterization of the excavation disturbed zone in the Opalinus Clay of the Mont Terri Rock Laboratory, *Eng. Geol.,* **66,** 9–38.

Bossart, P., Trick, T., Meier, P.M. & Mayor, J.C., 2004. Structural and hydrogeological characterisation of the excavation-disturbed zone in the Opalinus Clay (Mont Terri Project, Switzerland), *Appl. Clay Sci.,* **26,** 429–448.

Brady, B.H.G & Brown, E.T., 1993. *Rock Mechanics for Underground Mining*, Chapman & Hall.

Cabrera, J., Volant, P., Baker, C., Pettitt, W. & Young, R.P., 1999. Structural and geophysical investigations of the EDZ (Excavation Disturbed Zone) in indurated argillaceous media: the tunnel and the galleries of the IPSN Tournemire site (France), in *Rock Mechanics for Industry (Proceedings of the 37th U.S. Rock Mechanics Symposium*, Vail, Colorado, June), Vol. **2,** pp. 957–964, eds Amadei, B., Kranz, R.L., Scott, G.A. & Smeallie, P.H., Balkema.

Cai, M., Kaiser, P.K. & Martin, C.D., 2001. Quantification of rock mass damage in underground excavations from microseismic event monitoring, *Int. J. Rock Mech. Min. Sci.,* **38,** 1135–1145.

Chow, T.M., Meglis, I.L. & Young, R.P., 1995. Progressive microcrack development in tests on Lac du Bonnet granite II. Ultrasonic tomographic imaging, *Int. J. Rock Mech. Min. Sci. Geomech. Abstr.,* **32,** 751–761.

David, C., Robion, P. & Menéndez, P., 2007. Anisotropy of elastic, magnetic and microstructural properties of the Callovo-Oxfordian argillite, *Phys. Chem. Earth,* **32,** 145–153.

Falls, S.D. & Young, R.P., 1998. Acoustic emission and ultrasonic-velocity methods used to characterise the excavation disturbance associated with deep tunnels in hard rock, *Tectonophysics,* **289,** 1–15.

Feignier, B. & Young, R.P., 1992. Moment tensor inversion of induced microseismic events: evidence of non-shear failures in the $-4 < M < -2$ moment magnitude range, *Geophys. Res. Lett.,* **19,** 1503–1506.

Forney, F., 1999. Caractérisation par méthodes ultrasoniques de la zone endommagée (EDZ) induite par le creusement d'un tunnel en milieu argileux: Cas d´étude au tunnel du Mont Terri, *PhD thesis*, Institut National Polytechnique de Lorraine, Switzerland.

Gutenberg, B. & Richter, C.F., 1944. Frequency of earthquakes in California, *Bull. seism. Soc. Am.,* **34,** 185–188.

Hudson, J.A., Pearce, R.G. & Rogers, R.M., 1989. Source type plot for inversion of the moment tensor, *J. geophys. Res.,* **91,** 765–774.

Jaeger, J.C. & Cook, N.G.W., 1979. *Fundamentals of Rock Mechanics*, Chapman & Hall.

Jakubick, A.T. & Franz, T., 1993. Vacuum testing of the permeability of the excavation damaged zone, *Rock Mech. Rock Eng.,* **26,** 165–182.

Jones, S.M., 1995. Velocity and quality factors of sedimentary rocks at low and high effective pressures, *Geophys. J. Int,* **123,** 774–780.

Kayal, J.R., 2008. *Microearthquake Seismology and Seismotectonics of South Asia*, Springer.

Le Gonidec, Y. *et al.*, 2012. Field-scale acoustic investigation of a damaged anisotropic shale during a gallery excavation, *Int. J. Rock Mech. Min. Sci.,* **51,** 136–148.

Lei, X., Kusunose, K., Rao, M.V.M.S., Nishizawa, O. & Satoh, T., 2000. Quasistatic fault growth and cracking in homogeneous brittle rock under triaxial compression using acoustic emission monitoring, *J. geophys. Res.,* **105,** 6127–6139.

Lei, X., Nishizawa, O., Kusunose, K. & Satoh, T., 1992. Fractal structure of the hypocenter distributions and focal mechanism solutions of acoustic emission in two granites of different grain sizes, *J. Phys. Earth,* **40,** 617–634.

Lemaître, J., 1990. Micro-mechanics of crack initiation, *Int. J. Fract.,* **42,** 87–99.

Lockner, D.A., Byerlee, J.D., Kuksenko, V., Ponomarev, A. & Sidorin, A., 1991. Quasi-static fault growth and shear fracture energy in granite, *Nature,* **350,** 39–42.

Lynch, R.A. & Mendecki, A.J., 2001. High-resolution seismic monitoring in mines, in *Rockbursts and Seismicity in Mines-RaSiM5*, pp. 19–24, eds van Aswegan, G., Durrheim, R.J. & Ortlepp, W.D., South African Institute of Mining and Metallurgy.

Maineult, A. *et al.*, 2013. Anomalies of noble gases and self-potential associated with fractures and fluid dynamics in a horizontal borehole, Mont Terri Underground Rock Laboratory, *Eng. Geol.,* **156,** 46–57.

Martin, C.D., 1997. Seventeenth Canadian Geotechnical Colloquium: the effect of cohesion loss and stress path on brittle rock strength, *Can. Geotech. J.,* **34,** 698–725.

Martin, C.D., Lanyon, G.W., Bossart, P. & Blümling, P., 2004. Excavation disturbed zone (EDZ) in clay shale: Mont Terri, Unpublished Mont Terri Technical Report.

Martino, J.B. & Chandler, N.A., 2004. Excavation-induced damage studies at the underground research laboratory, *Int. J. Rock Mech. Min. Sci.,* **41,** 1413–1426.

Maxwell, S.C. & Young, R. P., 1996. Seismic imaging of rock mass responses to excavation, *Int. J. Rock Mech. Min. Sci. Geomech. Abstr.,* **33,** 713–724.

McGarr, A. & Simpson, D., 1997. A broad look at induced and triggered seismicity, in *Rockbursts and Seismicity in Mines*, pp. 385–396, eds Lasocki, S. & Gibowicz, S., Balkema.

Nelder, J. & Mead, R., 1965. A simplex method for function minimisation, *Comput. J.,* **7,** 308–312.

Nicollin, F., Gibert, D., Lesparre, N. & Nussbaum, C., 2010. Anisotropy of electrical conductivity of the excavation damaged zone in the Mont Terri Underground Rock Laboratory, *Geophys. J. Int.,* **181,** 303–320.

Nussbaum, C., Bossart, P., Amann, F. & Aubourg, C., 2011. Analysis of tectonic structures and excavation induced fractures in the Opalinus Clay, Mont Terri underground rock laboratory (Switzerland), *Swiss J. Geosci.,* **104,** 187–210.

Pettitt, W.S., 1998. Acoustic emission source studies of microcracking in rock, *PhD thesis*, Keele University, Keele, Staffordshire, UK.

Pettitt, W.S., Baker, C., Collins, D.S. & Young, R.P., 2003. InSite Seismic Processor User Operations Manual Version 2.10, Applied Seismology Consultants Ltd.

Poplawski, R.F., 1997. Seismic parameters and rockburst hazard at Mt Charlotte mine, *Int. J. Rock Mech. Min. Sci.,* **34,** 1213–1228.

Press, W.H., Flannery, B.P., Teukolsky, S.A. & Vetterling, W.T., 1994. *Numerical Recipes in C: The Art of Scientific Computing*, 2nd edn, Cambridge Univ. Press.

Rao, M.V.M.S. & Kusunose, K., 1995. Failure zone development in andesite as observed from acoustic emission locations and velocity changes, *Phys. Earth planet. Inter.,* **88,** 131–143.

Sarout, J., Ougier-Simonin, A., Guéguen, Y. & Schubnel, A., 2010. Active and passive seismic monitoring of shales under triaxial stress conditions in the laboratory, in *Proceedigns of the EAGE Shale Workshop 2010: Shale—Resource & Challenge*, 2010 April 26–28, Nice, France.

Sato, T., Kikuchi, T. & Sugihara, K., 2000. In-situ experiments on an excavation disturbed zone induced by mechanical excavation in Neogene sedimentary rock at Tono mine, central Japan, *Eng. Geol.,* **56,** 97–108.

Scholz, C.H., 1968. Experimental study of the fracturing process in brittle rock, *J. geophys. Res.,* **73,** 1447–1454.

Schubnel, A., Nishizawa, O., Masuda, K., Lei, X.J., Xue, Z. & Guéguen, Y., 2003. Velocity measurements and crack density determination during wet triaxial experiments on Oshima and Toki granites, *Pure appl. Geophys.,* **160,** 869–887.

Senfaute, G., Chambon, C., Bigarre, P., Guise, Y. & Josien, J.P., 1997. Spatial distribution of mining tremors and the relationship to rockburst hazard, *Pure appl. Geophys.,* **150,** 451–459.

Šílený, J. & Milev, A., 2008. Source mechanism of mining induced seismic events: resolution of double couple and non double couple models, *Tectonophysics,* **456,** 3–15.

Souley, M., Homand, F., Pepa, S. & Hoxha, D., 2001. Damage-induced permeability changes in granite: a case example at the URL in Canada, *Int. J. Rock Mech. Min. Sci.,* **38,** 297–310.

Spottiswoode, S.M., 1988. Total seismicity and the application of ESS analysis to mine layouts, *J. S. Afr. Inst. Min. Metall.,* **88,** 109–116.

Szwedzicki, T., 2003. Rock mass behaviour prior to failure, *Int. J. Rock Mech. Min. Sci.,* **40,** 573–584.

Thury, M. & Bossart, P., 1999. The Mont Terri rock laboratory, a new international research project in a Mesozoic shale formation, in Switzerland, *Eng. Geol.,* **52,** 347–359.

Tsang, C.F., Barnichon, J.D., Birkholzer, J., Li, X.L., Liu, H.H. & Sillen, X., 2012. Coupled thermo-hydro-mechanical processes in the near field of a high-level radioactive waste repository in clay formations, *Int. J. Rock Mech. Min. Sci.,* **49,** 31–44.

Wassermann, J., Senfaute, G., Amitrano, D. & Homand, F., 2009. Evidence of dilatant and nondilatant damage processes in oolitic iron ore: P-wave velocity and acoustic emission analyses, *Geophys. J. Int.,* **177,** 1343–1356.

Wassermann, J., Sabroux, J.C., Pontreau, S., Bondiguel, S., Guillon, S., Richon, P. & Pili, E., 2011. Characterization and monitoring of the excavation damaged zone in fractured gneisses of the Roselend tunnel, French Alps, *Tectonophysics,* **503,** 155–164.

Weiss, J., 2003. Scaling of fracture and faulting of ice on Earth, *Surv. Geophys.,* **24,** 185–227.

Yong, S., Kaiser, P.K. & Loew, S., 2010. Influence of tectonic shears on tunnel-induced fracturing, *Int. J. Rock Mech. Min. Sci.,* **47,** 894–907.

Young, R.P. & Collins, D.S., 2001. Seismic studies of rock fracture at the underground research laboratory Canada, *Int. J. Rock Mech. Min. Sci.,* **38,** 787–799.

Young, R.P., Hazzard, J.F. & Pettitt, W.S., 2000. Seismic and micromechanical studies of rock fracture, *Geophys. Res. Lett.,* **27,** 1767–1770.

Young, R.P., Maxwell, S.C., Urbancic, T.I. & Feignier, B., 1992. Mining-induced microseismicity: monitoring and applications of imaging and source mechanism techniques, *Pure appl. Geophys.,* **139,** 697–719.

Zang, A., Wagner, F.C., Stanchits, S., Janssen, C. & Dresen, G., 2000. Fracture process zone in granite, *J. geophys. Res.,* **105,** 23 651–23 661.

Zhang, C.L., 2011. Experimental evidence for self-sealing of fractures in claystone, *Phys. Chem. Earth, Parts A/B/C,* **36,** 1972–1980.

Zhang, C.L. & Rothfuchs, T., 2008. Damage and sealing of clay rocks detected by measurements of gas permeability, *Phys. Chem. Earth, Parts A/B/C*, **33,** S363–S373.